

SLAC-PUB-2181  
August 1978  
(E/I)

A LARGE CYLINDRICAL DRIFT CHAMBER FOR  
THE MARK II DETECTOR AT SPEAR\*

W. Davies-White, G. E. Fischer, M. J. Lateur, R. H. Schindler,  
R. F. Schwitters, J. L. Siegrist, H. Taureg, and H. Zacconet

Stanford Linear Accelerator Center  
Stanford University, Stanford, California 94305

D. L. Hartill  
Cornell University  
Ithaca, New York 14850

ABSTRACT

We describe a large cylindrical drift chamber designed for the Mark II magnetic detector at the SLAC  $e^+e^-$  storage ring SPEAR. Details on the mechanical construction, electronics readout, and measurements of chamber efficiencies and precision are presented.

(Submitted to Nucl. Instrum. Methods.)

---

\*Work supported by the Department of Energy.

†On leave from CEN Saclay, F91 190 Gif-sur-Yvette, France.

## Introduction

We have built a large cylindrical drift chamber for the Mark II detector which is now operating at the SLAC  $e^+e^-$  storage ring SPEAR. The drift chamber serves as the central detection device for charged particles produced in  $e^+e^-$  annihilations. Figure 1 shows a general outline of the detector. The chamber is placed inside a 4 kG solenoidal magnetic field which is parallel to the beam directions thus allowing the measurement of charged particle momenta from the curvature of their tracks inside the chamber. The electric field in the drift cells is perpendicular to the magnetic field. We have chosen not to use Lorentz force compensating field wires in order to simplify the design and construction<sup>1,2)</sup>. In this drift chamber only 3 field wires per drift cell, each held at the same potential, are used for shaping the electric field. The chamber contains 3204 drift cells arranged in 16 concentric, cylindrical layers enclosed in a common gas volume. To obtain a position measurement along the beam direction 10 layers have their wires oriented at a small stereo angle with respect to the chamber axis.

In the following, we describe first the geometrical and electrical parameters of the drift chamber. Next, we discuss the properties of the gas mixture used and the construction of the chamber. An outline of the readout electronics follows in the next section. Finally, we summarize our experiences after 9 months operation of the chamber at SPEAR and measurements of chamber efficiencies and resolution.

## Design Description

### Geometry

The drift chamber is enclosed in a cylindrical can of 1.51 m outer and 0.37 m inner radius with a length of 2.85 m (see fig. 2). The central

open region accommodates the beam pipe with vacuum pumps and scintillation counters used in the triggering of the detector. It also allows for the addition of more wire chambers in the future. The conical sections in the two end plates provide room for the compensating magnets.

The 3204 drift cells are, as already mentioned, arranged in 16 concentric, cylindrical layers. The cells in the inner 6 layers have one-half the drift space in the azimuthal direction as the cells of the outer 10 layers. This allows for the decrease in track density at greater radial distances from the interaction point. To obtain a position measurement along the beam direction, 10 layers have their wires oriented at about  $\pm 3$  degrees with respect to the chamber axis. The innermost layer contains axial wires and is followed by layers of positive and negative stereo angle. This pattern repeats itself, leaving the outermost layer an axial one.

The wire pattern repeats in 30-degree intervals of azimuthal angle in all layers starting with the field wires of all cells in all 16 layers on the same radial line (see fig. 3(a)). The radii, numbers of cells per layer, and stereo angles are compiled in table 1. We number the layers from 6 to 21 starting at the smallest radius, as in this table.

Each drift cell consists of 3 field wires and a sense wire. The dimensions of both types of drift cells are shown in fig. 3(b). The distance between the nearest field wire and the sense wire is 18.03 mm for the large cells and 9.01 mm for the small cells. All cells have the same heights of 11.99 mm. The cells are slightly tapered since the field wire triplets are located on radial lines. The opening angle of these radial lines through adjacent wire triplets varies between 1.4 and 2.5 degrees.

### Electrical Structure

In our design, the number of field wires is kept to a minimum, thus simplifying the construction of the chamber. As a consequence, no field shaping is done to compensate the Lorentz force by either tilting the field wires with respect to the center plane of a drift cell or keeping the field wires at different potentials. All field wires in one layer are held at one common potential which is negative with respect to ground-- for the small cell layers -2.95 kV and for the large cell layers -3.5 kV. The sense wires are at ground potential, thus avoiding the need for HV capacitors to couple preamplifiers to signal wires. Figure 4 shows contours of equal magnitude of the electric field  $\vec{E}$  for both cell sizes. In fig. 5 the magnitude of the electric field is plotted along a line between the sense wire and the nearest field wire. The large cells exhibit the expected greater variations of the electric field in the drift space.

### Wires

The field wires have a diameter of 152.4  $\mu\text{m}$  (0.006 inch) whereas the diameter of the sense wires is 38.1  $\mu\text{m}$  (0.0015 inch). Both types of wire are made out of a copper beryllium alloy (95% Cu, 5% Be) with a silver plating. The decision to use a 40  $\mu\text{m}$  thick sense wire instead of a 20  $\mu\text{m}$  wire stems principally from the desire to achieve a higher electric field in the drift cells at larger distances from the sense wire. In fig. 6, contours of constant drift velocity in the absence of a magnetic field for 20  $\mu\text{m}$  and 40  $\mu\text{m}$  diameter sense wires are plotted for the large cells. In the large cells there are significantly smaller variations in the local velocity near the field wires for the 40  $\mu\text{m}$  sense wires than for a 20  $\mu\text{m}$  sense wire. Contours of constant drift velocity for the small drift

cells are shown in fig. 7 for a 40  $\mu\text{m}$ -thick sense wire. In addition, the large diameter allowed the use of a Cu-Be alloy which has desirable mechanical properties. This wire can be stretched by up to 50% of its original length before breaking (50% elongation under  $\sim 3 \text{ t/cm}^2$  which is roughly half the tensile strength). We will come back to this point later in the description of the chamber construction.

The thicker sense wire has the disadvantage of a much smaller gas amplification region in comparison with the 20  $\mu\text{m}$ -thick wire at the same potential of the field wires. The same gain in the gas can then only be reached by a higher potential difference between field wires and signal wires. In our configuration the voltage had to be changed from -2.2 kV to -2.9 kV in a test chamber when going from the 20  $\mu\text{m}$  to the 40  $\mu\text{m}$  sense wire in the small cells.

#### Gas Mixture

The drift chamber uses a 1 to 1 Argon-Ethane gas mixture which is supplied premixed to a semiclosed gas recirculation and cleaning system operated above atmospheric pressure ( $\sim 1 \text{ g cm}^2$  overpressure). Approximately 1250 liters per hour of the  $\sim 18 \text{ m}^3$  gas volume are passed over a palladium catalyst and through a molecular sieve to remove oxygen as water vapor. The catalyst requires us to bleed hydrogen into the chamber at  $\sim 60 \text{ cm}^3/\text{h}$ . The oxygen level is maintained at  $\sim 50 \text{ ppm}$ . Before returning to the chamber, the gas passes through a 50  $\mu\text{m}$  filter to remove any large contaminants. Fresh gas is added to the system at a rate of  $\sim 170$  liters per hour. The selection of the gas mixture was made taking into account several constraints. These included maximum drift times set by the primary trigger, the small average electric field in the large cells, and the synchrotron radiation background of the SPEAR environment.

The maximum drift time is  $\sim 430$  nsec which is set by readout and trigger requirements derived from a 780-nsec-long interval between beam crossings. With our geometry in the large drift cells this leads to a lower bound on the average drift velocity of  $\sim 4.5$  cm/ $\mu$ sec. This velocity must be achieved in the presence of the small average electric field in the large cells (as shown in fig. 5), and the 4.1 kG magnetic field parallel to the wires.

Under these constraints we looked for a gas which had a large drift velocity, close to saturation in the region above approximately 600 V/cm. We also desired a gas that is not extremely sensitive to fluctuations in concentration so that a simple gas system could be used. Using test chambers, Argon-Ethane, Argon-Ethylene, and Argon-Isobutane-Methylal mixtures were studied. At the time of our search, measurements were available only on the last two mixtures<sup>3,4,5</sup>). A velocity monitor was constructed to measure the drift velocity versus electric field without a magnetic field. Figure 8 shows a schematic of the monitor. Within the drift space a very uniform electric field is created by the shaping wires. Two Am<sup>241</sup> sources provide  $\alpha$  particles which are collimated by narrow defining slits and traverse the drift space, triggering one of the two matched proportional wire detectors P1 or P2. The slits are at a known separation  $D_{12}$ . The passage of  $\alpha$  particles ionizes the gas and generates a distribution of electrons which drift towards the end detector P3. Two independent distributions of arrival times are measured: The time elapsed between P1 and P3 firing, and P2 and P3 firing. The drift velocity is then calculated simply as the difference in the mean of these time distributions divided by  $D_{12}$ . An accuracy in drift velocity of better than  $\pm 2\%$  has been achieved with limitations being principally mechanical.

Figure 9 shows measurements of drift velocity versus electric field with this apparatus on several gas mixtures. Argon-Ethane mixtures appeared to satisfy our requirement for speed and saturation. In addition, it appears less sensitive to fluctuations in concentration. We observed changes in the drift velocity of less than 2% for a change of almost 20% in the Argon concentration. More recent measurements find similar results<sup>6)</sup>.

Finally, Ethane has a rather stable single carbon bond, making polymerization less likely in the synchrotron radiation background at SPEAR. As a test we irradiated a small test chamber ( $15 \times 15 \times 2 \text{ cm}^3$ ) for 10 days with a 250 Ci  $\text{Co}^{60}$  source and examined the wires afterwards. The high voltage in the chamber was held at the operating point and the gas was exchanged at a rate of  $\sim 1$  chamber volume per hour during the test. We could not detect any deposits on the wires.

From fig. 9 it is clear that the drift velocity is never well saturated over the entire area of the cell even when using an Argon-Ethane mixture. In order to simplify the chamber construction we have taken the philosophy of performing the necessary corrections for this effect and for the effect of the magnetic field in our offline analysis programs. We will come back to this in the last section of this paper.

### Construction

The end plates of the chamber have been constructed in two sections (see fig. 2). The inner part (the conical section) has been manufactured from a solid, 6.35 mm-thick aluminum cone (inner radius 37.94 cm, outer radius 64.45 cm, height 49.05 cm) having a flat rim at the outer radius. Layer 6 to 9 are located in the conical portion whereas the remaining

small cell layers, 10 and 11, are in the flat part. The outer portion of the end plate for the large-cell layers consists of an aluminum honeycomb, 7.62 cm-thick, with an inner radius of 78.74 cm and an outer radius of 150.90 cm. Twelve pie-shaped aluminum plates, 1.59 mm-thick, with precision drilled holes (to  $\pm 50 \mu\text{m}$ ) to position the wires, have been glued to both faces of the honeycomb. The use of the honeycomb allowed a reduction in the number of radiation lengths in the end plate by a factor of about 5 over a solid aluminum plate thus minimizing the amount of material in front of the endcap shower counters of the Mark II detector. The material in the end plate of the drift chamber amounts to about 20% of a radiation length.

The outer cylindrical can of the chamber is made out of 6 aluminum plates, 6.25 mm-thick, 150.90 cm radius, which support the load from the wires in the chamber. Fiberglass on the outside of the aluminum can provides a gas seal and adds to the rigidity of the can preventing torsion. The inner cylindrical gas seal (radius 37.94 cm and 3.18 mm thick) consists of a clear plastic material (Lexan) allowing inspection of the chamber interior.

The gas is supplied through two toroidal manifolds on one end of the chamber, one between layers 10 and 11, the other one between layer 21 and the outside wall. Two similar manifolds at the corresponding positions on the opposite end plate serve as gas outlets.

The feedthroughs which hold the wires in place (shown in fig. 10) are screw-machined plastic pieces (Delrin), each with a brass insert. The position of a wire is determined by its location at the circumference of the 0.375 mm-wide hole in the brass insert (see insert in fig. 10). Epoxy secures the wire in place and serves as a gas seal.



The wires have been strung by hand in a clean-room beginning in layer 6 with both end plates about 3.8 cm nearer each other than in the final configuration. Six support rods with jack screws for stretching the wires held the end plates at the outer circumference of the chamber during the wire stringing. After insertion of the wires in layers 6 to 11 the distance between the end plates was increased by approximately 1.3 cm. The remaining layers 12 to 21 were then strung. The wires were stretched another  $\sim 2.5$  cm beyond their elastic limit to their final length and tension. The mechanical properties of the Cu-Be wire allowed this stretching process (in contrast to tungsten wire). In this construction technique, the deformation of the end plates under the load of the wires is automatically taken into account and a preloading of the end plates necessary when using tungsten wires can be avoided. At the inner radius of the chamber, the end plates are deflected by approximately 8 mm under the load of the wires. The inner Lexan gas seal and the outer aluminum were installed after the stretching of all wires and the support rods were then removed.

#### Electronics

As indicated in fig. 11, signals from each sense wire are carried through 2 to 4 meters of  $50 \Omega$  coaxial cable to a front-end circuit employing a LeCroy LD604 discriminator and preamp. The preamplifier inputs are terminated in  $100 \Omega$ , and thresholds are set to typically 500  $\mu\text{V}$ . The LD604 are mounted 16 to a board with the boards placed in cages mounted directly on the face of the detector outside the magnetic field. After a 100 hour burn-in period prior to installation, we had less than 0.25% failures during the first nine months of operation.

The differential output signal from the LD604 is carried by 25 m of twisted pair to the time-to-amplitude converter (TAC) as shown in fig. 11. The preamp signals serve as the start input and a common stop is derived from a delayed beam crossing signal. The TAC's process chamber data in three ways. First, they produce a fast OR signal which is true if any of the 32 channels in the TAC module had a start input for use in the primary trigger. Second, these start inputs are parallel loaded into shift registers for use in the secondary trigger<sup>7)</sup>. Finally, the TAC produces an analog signal for each input channel proportional to the time between the first start and the common stop<sup>8)</sup>. No provision is made to encode multiple hits. All the analog outputs in one CAMAC crate (up to  $32 * 19 = 608$ ) are digitized by a single ADC in the crate which is part of the brilliant ADC (BADC) readout system. Details concerning the BADC readout system can be found in ref. <sup>9)</sup>. Briefly, the BADC has a 16-bit microprocessor, employing 4 AMD2901 4-bit slices, which determines which channels have outputs above a threshold, preselected for each channel. For such a channel, the BADC corrects the output voltage of the TAC for an offset and a gain, yielding a drift time which is stored with a channel label in the 4k-memory of the BADC. In this manner, the host computer (Xerox Sigma-5) needs only to address the BADC itself in order to process the data from an entire CAMAC crate of drift chamber channels. There are 6 such crates in the system for our 3204 drift cells.

High voltage is supplied to the field wires by 16 channels of DANFYSIK model N1130 power supplies. Each channel separately controls one drift chamber layer. A distribution box on the end face of the detector contains current limiting resistors and serves to fan out the

voltage to each high voltage segment of 12 (for the large cell layers) or 24 (for the small cell layers) triplets of field wires (fig. 12). The high voltage distribution was split into groups mainly to achieve an isochronous distribution of calibration pulses and to facilitate the isolation of short circuits and discharges.

In addition, provision has been made to capacitively couple a signal (approximately 5 V, 8 nsec risetime) onto the high voltage lines at the distribution box in order to provide calibration pulses for all channels. The pulse shape and risetime is preserved at the chamber by the use of impedance matching strip lines which distribute the high voltage at the chambers. This timed signal is the output of a fast amplifier, triggered by one pulse of a pulse pair generator, the other pulse of the pair going to create the common stop for the TAC's. The coupling of the signal on the high voltage wires to the sense wires is about 0.1% or approximately 10 times the threshold setting of the LD604. By varying the time separation in the pulse pair, the gains and offsets of all TAC channels can be determined up to an overall "event" start time. The constants so determined are then fed back into the BADC memory for converting raw ADC counts into drift times during normal data taking. By studying the results of calibration runs, the overall time resolution of the electronics system has been determined to be about 900 psec (standard deviation). Using an average drift velocity of 5 cm/ $\mu$ sec this implies a contribution to the spatial resolution of 45  $\mu$ m. The calibration pulses provided a very useful tool for debugging and monitoring the readout electronics for the drift chamber.

### Operation of the Chamber

During and shortly after the stretching of the chamber to its final dimensions, approximately 30 sense wires broke. This is thought to have been caused by sharp edges (burrs) at the transition from the conical to the cylindrical part of the hole in the brass insert of the feedthrough because almost all wires broke in that region. During the transport of the chamber from the construction site to SPEAR, a few wires broke for the same reason.

Some loose wires were also found during the initial checkout of the chamber. We believe that the wires slipped through the epoxy which had not completely cured in these cases. Most of these wires broke from sparking before they could be located. Unfortunately, the original HV-distribution network allowed too large a potential difference between neighboring HV segments within one layer so that some sense wires at the boundary of two HV segments broke in addition, as a consequence of a short circuit from a broken wire elsewhere in that layer. This problem was encountered only in the small cell layers where the equilibrium between the wire tension and the electrostatic forces is much more critical than in the large drift cells, because of the higher average electric field in the small drift cells. Most of the broken wires were replaced by the following technique before data taking began.

First, the broken wire and its feedthroughs are removed. Then a neighboring field wire is stretched 10 to 20 cm by removing its feedthroughs. Two wires are attached to it. These two wires are pulled through the chamber and one of them is transferred with the help of a hook to the holes in both end plates that originally positioned the

broken wire. Finally, new wires are pulled through and fastened by new feedthroughs. During the last five months of continuous operation we have not had any broken sense wires.

A more serious problem in the form of a self-sustaining glow discharge in one region of the chamber was encountered after several weeks of operation with beams in the storage ring. Running at high beam energies and large beam currents initiated this effect. To stop the discharge we had to lower the potential difference between sense and field wires by approximately 1.0 kV in the worst cases. As a consequence an azimuthal segment occupying approximately  $30^\circ$  in three layers was no longer operational. The reason for the discharges has been traced to some high dielectric strength epoxy which was accidentally splattered over some of the field wires during the chamber construction. We could reproduce the effect in a small test chamber where we deliberately "dirtied" some wires with epoxy. A mechanism for discharges through a dielectric was described by L. Malter in 1936 (ref. 10). To solve the problem all wires in the affected region have been replaced by clean wires.

Operating the chamber without the magnet powered and with the end-caps of the detector removed causes an increase of the current in the high voltage system, due to high humidity and the resultant leakage currents at the outside of the chamber. Under normal operating conditions with a powered magnet, humidity poses no problem because of the higher ambient temperatures inside the detector. To alleviate the problem the end faces of the chamber with the high voltage distribution network have been put in a dry nitrogen atmosphere.

At beam energies above 3.3 GeV, synchrotron radiation leaking into the drift chamber contributes significantly to the residual ionization

in the chamber gas. This results in large currents measured in the high voltage system, however, the noise rate in events is not increased. We are currently studying the effect on wire surfaces when heavy ionization is present and the possibilities to suppress the synchrotron radiation reaching the chamber by masks and changes in the beam orbits.

### Performance

The space-time relationship, resolution, and efficiency of the drift chamber have been studied using events collected in the Mark II. There are two levels of track finding, reconstruction, and fitting. The first level uses roads from the secondary trigger logic<sup>7)</sup> to rapidly associate "hit" wires into track candidates. Whenever possible, the left-right ambiguity at each layer is resolved by a simple fit to a circle in projection. At this level, drift times are converted to distances by a linear space-time relation, where the distance is taken to be the distance of closest approach to the sense wire, with an angle estimate based on the initial estimate of curvature from the secondary trigger logic road. The results are then passed to a second level of reconstruction where these tracks are refit, taking into account the inhomogeneities of the magnetic field, multiple scattering, and further refinements in the space-time relation, in an iterative least-squares fit which results in improved estimates of particle position, direction and momentum. At this final level, a more sophisticated algorithm searches for tracks either not previously found, or incorrectly resolved because the linear space-time relation proved a poor approximation at the initial level. The track finding efficiency averages ~96% at present.

The space-time relation has been studied in detail in the presence of the 4.1 kG magnetic field. Several thousand hadronic events collected over approximately 4 days of actual running provided a track sample with a wide distribution of curvatures. Tracks within this sample fell in the range of  $\pm 50$  degrees from normal incidence to the cells.

Figure 13 shows the measured time-distance relation observed in both the small and large cells for different values of the incidence angle. The determination of this relationship is discussed below. The distance plotted is the distance of closest approach (DCA) to the sense wire. This variable is useful because the electric field is predominantly radial near the sense wire (fig. 4). One immediately notes the  $\pm$  asymmetry in the time-distance relation. This asymmetry originates from the distortion of the drift path as a result of the Lorentz force. The symmetry of the effect follows the sign of the incidence angle (see fig. 14), independent of the side of the wire. For negative angles, the Lorentz force will tend to lengthen the path, while for positive angles it will shorten them relative to the zero field case. Within 5 mm of the sense wires the electric field dominates, and drift times appear essentially unaffected by the presence of the magnetic field and almost linearly related to the distance of closest approach. At larger distances for negative incidence angles, the drift path is in the region of lower electric field outside of the cell's median plane. Since the drift velocity is not saturated over the entire cell, and because of the Lorentz force, we measure substantially larger drift times. At large negative angles and large distances, corrections for these nonlinear effects amount to as much as 40% of the linear terms. For positive angles the Lorentz

force focuses electrons onto the median plane, both shortening the drift path, and leading through regions of higher electric field. This results in a reduction in the size of the nonlinear and angle-dependent terms in the space-time relation.

The functional form of the space-time relation was chosen on the basis of the field shape, drift velocity, and the resulting trajectories in the cells. The form is a quadratic polynomial representing an effective velocity, which can be multiplied by the measured drift time (after time-of-flight and wire propagation corrections) to determine the distance of closest approach. The coefficients are dependent on the incidence angle, only for measured times greater than approximately 100 nsec. This reflects the deviation from a purely radial electric field far from the sense wire. No dependence on polar angle of the track is observed.

The coefficients are determined by a self-consistent, iterative approach. The average spatial residual,  $\langle \Delta \rangle$  (where  $\Delta$  is the deviation of a fitted track from the position associated with its drift time) is determined as a function of measured drift time using estimates for the coefficients. This residual is directly related to changes in the coefficients of the space-time parametrization, which we wish to determine. The coefficients are adjusted to minimize the mean residuals and the entire procedure is then iterated. This means that the sample of tracks are refit with the previous coefficients, mean residuals recalculated, and new coefficients determined. With good starting values, the coefficients converge after  $\sim 4$  iterations.

The spatial resolution of the drift chamber is simultaneously measured as the space-time relation is determined. The improvement in



resolution as the coefficients converge provides a test of the self-consistency of the method. Figure 15 shows the distributions of the space residual  $\Delta$  for various angles of incidence in both cell types, averaging over the track position within the cell. Figure 16 summarizes the widths ( $\sigma$  from the FWHM after removing the non-Gaussian tails) of these distributions as a function incidence angle. A weak angular asymmetry is still seen reflecting the presence of the magnetic field. The poorer resolution at larger angles results from the greater variations in drift path length outside of the median plane of the cell. Figure 17 shows the variation of the resolution as a function of distance of closest approach for normally incident tracks. We observe a rise near the sense wire presumably due to ionization statistics and a diffusion dominated increase at larger distances. At other angles the resolution follows a similar functional form and can be estimated by scaling the curves of fig. 17 with the angle dependence of fig. 16.

In fig. 18 we show a typical  $\chi^2$  distribution for tracks with momenta greater than 500 MeV/c. The spatial resolution in the fitting procedure was assumed to be 200  $\mu\text{m}$ . The curve superimposed is a theoretical  $\chi^2$  distribution. The average number of degrees of freedom in the data is 8. The data thus appear consistent with the assumed resolution, however, there is a long tail. We believe that the resolution may in fact improve because there are at this time no geometrical corrections to sense wire position in the track reconstruction. We are currently using the residuals to probe the physical plate and cone positions in the drift chamber to remove mechanical misalignments. These appear to be at the level of approximately 200  $\mu\text{m}$  in some layers. Once these geometrical

corrections are incorporated, the space-time relation will be reevaluated since it is inherently coupled to the geometry. We have found this iterative approach the only way to find a self-consistent solution to the two problems. Aside from geometrical effects, we attribute the remaining tail in part to in-flight decays of kaons and pions, which get reconstructed as a single track (approximately 1 out of 10 tracks decay within the chamber). Lastly, delta rays are suspected to contribute a large fraction of the drift times which are measured to be early relative to the track position in the cell. Work is proceeding in track reconstruction to remove questionable drift chamber hits and to find kinks resulting from decays.

The drift chamber efficiency is monitored continuously online using incoming data. The efficiency is determined on a cell by cell basis by finding how often a cell actually fired when a reconstructed track passes through it. Figure 19 shows plateau curves of reconstructed cosmic rays. Here the efficiency is measured by keeping all layers except the one in question at their normal voltage while varying the voltage of the layer in question. Layer 7 is a small cell layer and layer 15 has large cells. The chamber is operated at -2.9 kV for the small cells and -3.50 kV for the large cells. The innermost and outermost layers are operated somewhat higher because of their different electrostatic boundary conditions. The large cell plateau extends to approximately 3.9 kV and for the small cells to approximately 3.2 kV, again dependent on the physical boundary of the layer. The single cell efficiency of the chamber is above 99% at the operating point and is stable over periods of weeks.

Acknowledgements

We would like to thank M. Tonutti for his help in understanding the problem of discharges in the drift chamber and D. H. Miller for his contributions to the study of different field configurations in drift cells. We are grateful for the support of C. C. Noyer, R. K. Jobe and the technical staff at SLAC during the construction of the chamber, particularly the members of the Mechanical Fabrication Department under H. Zaiss. We are indebted to the Mark II collaboration for their contributions to the operation of the Mark II detector and to the data analysis system, especially W. Chinowsky, M. W. Coles, S. Cooper, A. D. Johnson, R. E. Millikan and G. H. Trilling who developed the track reconstruction.

References

- 1) B. Sadoulet and A. Litke, Nucl. Instrum. Methods 124 (1975) 349.
- 2) R. P. Thun and P. Kraushaar, University of Michigan preprint UM He 77-47 (1977, unpublished).
- 3) D. C. Cheng et al., Nucl. Instrum. Methods 117 (1974) 157.
- 4) A. Breskin et al., Nucl. Instrum. Methods 119 (1974) 9; 124 (1975) 189.
- 5) L. Christophorou, Atomic and Molecular Radiation Physics (Wiley, London, 1971).
- 6) H. Daum et al., "Measurements of electron drift velocities as a function electric and magnetic fields in several gas mixtures," CERN preprint (October 1977), to be published in Nucl. Instrum. Methods.
- 7) H. Brafman et al., "Fast track-finding trigger processor for the SLAC/LBL Mark II detector," Stanford Linear Accelerator Center preprint SLAC-PUB-2033 (1977).
- 8) E. L. Cisneros et al., "Drift chamber and pulse height readout system using analog multiplexing," Stanford Linear Accelerator Center preprint SLAC-PUB-1844 (1976).
- 9) M. Breidenbach et al., "Semi-autonomous controller for data acquisition, the brilliant ADC," Stanford Linear Accelerator Center preprint SLAC-PUB-2032 (1977).
- 10) L. Malter, Phys. Rev. 49 (1936) 478; see also for a wider discussion M. Bruining, Physics and Applications of Secondary Electron Emission (Pergamon Press, New York, 1954).

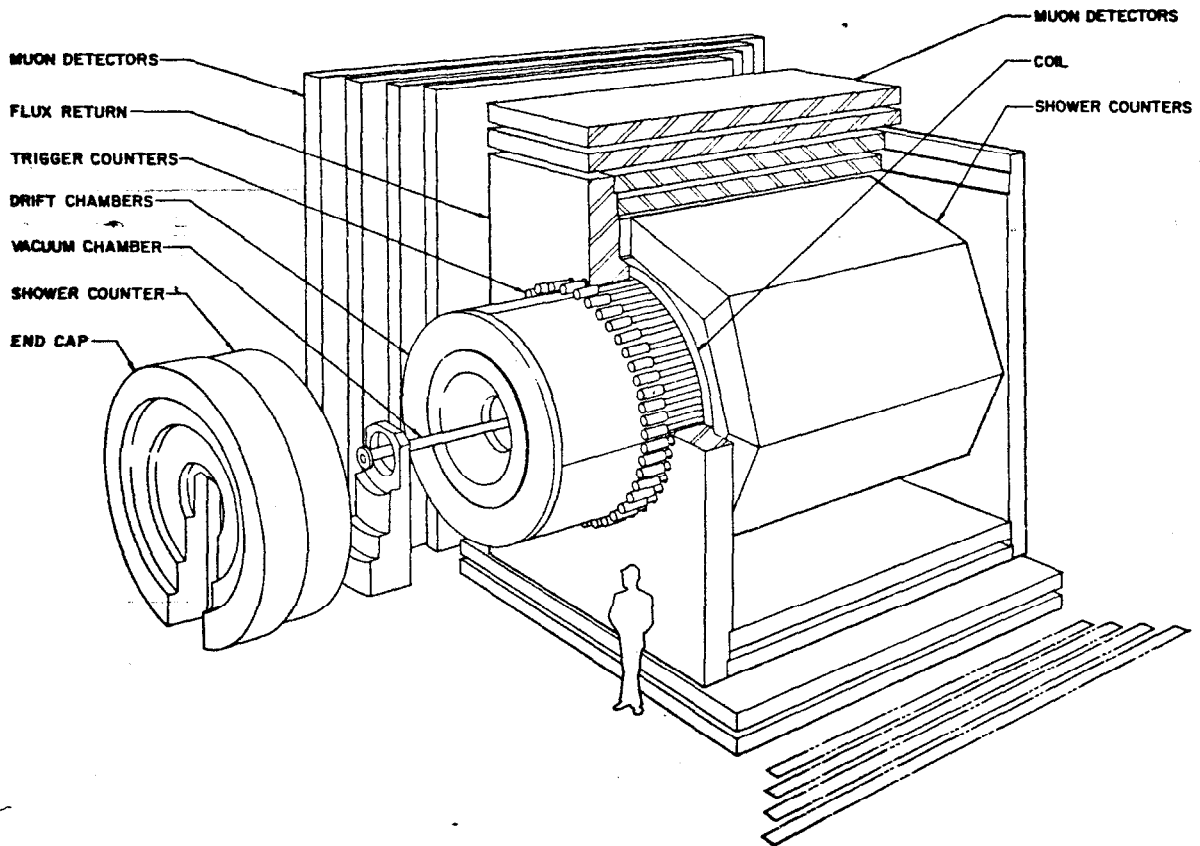
TABLE I

Layer Index (# of HV cables)	Radius (mm)	Active Length (mm)	Stereo Angle (degrees)	Number of Cells	Accumulated Material from Entrance to Drift Chamber System (including 3 mm Lexan window)	Fraction of rad. length ( $\times 10^{-3}$ )
					(mgm/cm <sup>2</sup> )	
6	413.6	1984.1	0	144	424	11.4
7	482.6	2222.9	+3.12	168	437	12.0
8	551.5	2461.7	-2.90	192	451	12.7
9	620.4	2700.5	0	216	464	13.3
10	689.4	2786.4	+2.90	240	478	13.9
11	758.3	2786.4	-2.90	264	491	14.5
12	827.2	2641.6	0	144	504	15.1
13	896.2	2641.6	+3.07	156	516	15.6
14	965.1	2641.6	-3.07	168	528	16.1
15	1034.0	2641.6	0	180	540	16.6
16	1103.0	2641.6	+3.07	192	552	17.2
17	1171.9	2641.6	-3.07	204	564	17.7
18	1240.8	2641.6	0	216	576	18.2
19	1309.8	2641.6	+3.07	228	589	18.7
20	1378.7	2641.6	-3.07	240	601	19.2
21	1447.7	2641.6	0	252	613	19.8

Figure Captions

1. Isometric view of the Mark II detector.
2. Construction drawing of the Mark II drift chambers; please note that all dimensions are in inches.
3. (a) Hole pattern for feedthroughs in the end plate. (b) dimensions-- in mm--of small and large drift cells.
4. Contours of equal magnitude of the electric field  $|\vec{E}|$ , the crosses mark the wire positions,  $|\vec{E}|$  changes by 50 V/cm between neighboring contours.  
(a) small cell, field wires at -2.85 kV  
(b) large cell, field wires at -3.40 kV
5. Magnitude of the electric field in the median plane of the drift cells. The distance between the sense wire and the nearest field wire is normalized to 1. The sense wire is at 1.
6. Contours of equal drift velocity for electrons in a large drift cell, field wires -3.4 kV, the velocity changes by 0.05 cm/ $\mu$ sec between neighboring lines, the crosses mark the wire positions.  
(a) 20  $\mu$ m sense wire  
(b) 40  $\mu$ m sense wires
7. Contours of equal drift velocity for electrons in a small drift cell, field wires -2.8 kV, the velocity changes by 0.05 cm/ $\mu$ sec between neighboring lines. The sense wire diameter is 40  $\mu$ m.
8. Schematic of apparatus for measuring electron drift velocities in gases.
9. Drift velocity versus electric field for different gas mixtures.
10. Feedthrough for wires in the flat part of the central section of the end plate.

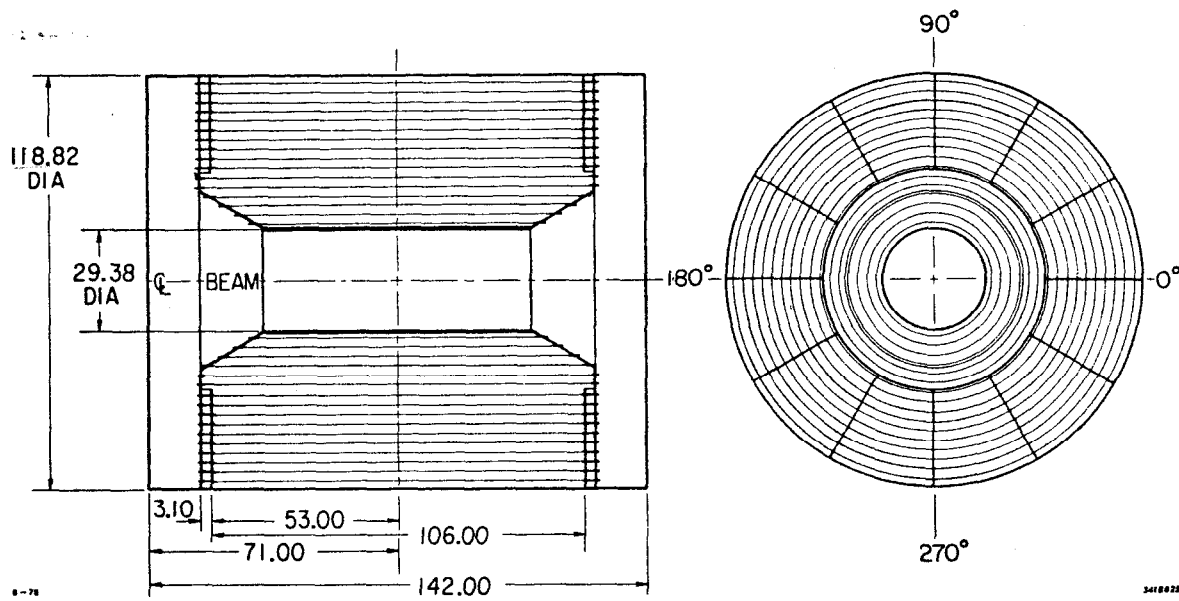
11. Scheme of the readout electronics.
12. Scheme of the high voltage system.
13. Drift time--distance of closest approach (DCA) relation for both the large and small cells.
14. Electron paths within a drift cell for different incidence angles of tracks.
15. Space residual  $\Delta$  for different incidence angles in the small and large drift cells.
16. Standard deviation  $\sigma$  of the space residual distributions as a function of incidence angle for both cell types. The curves are drawn to guide the eye.
17. Standard deviation  $\sigma$  of the space residual distributions for normally incident tracks as a function of distance of closest approach (DCA) to the sense wire. The distance between the sense wire and the cell boundary is normalized to 1. The curves are drawn to guide the eye.
18.  $\chi^2$  distribution for tracks with momenta greater than 0.5 GeV/c. The resolution was assumed to be 200  $\mu\text{m}$ . A  $\chi^2$  curve for 8 degrees of freedom is superimposed.
19. Efficiency  $\epsilon$  as a function of field wire potential U for two layers of the drift chamber. The curves are drawn to guide the eye.



7-78

3418A22

Fig. 1



8-78

3418B23

Fig. 2



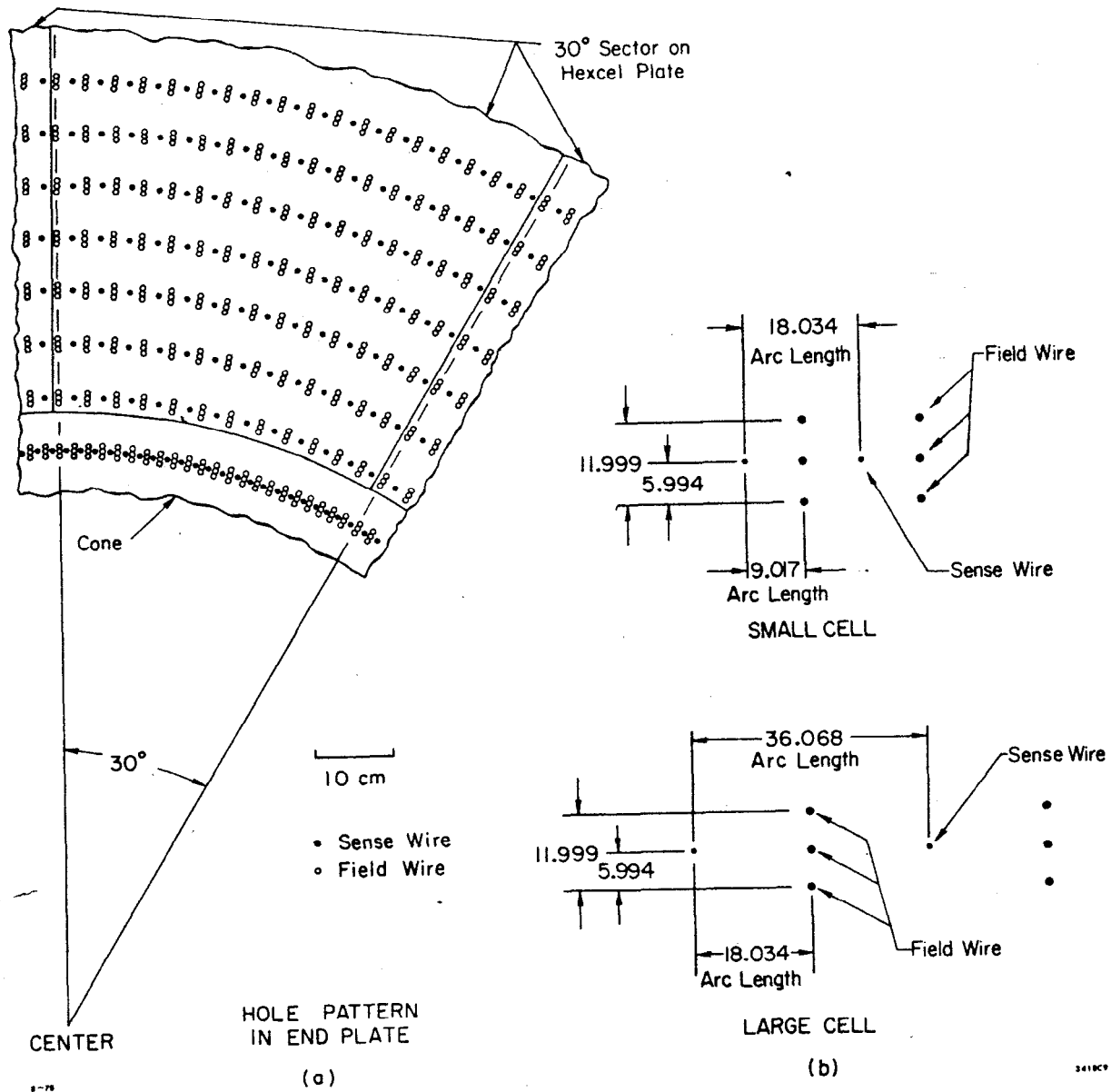
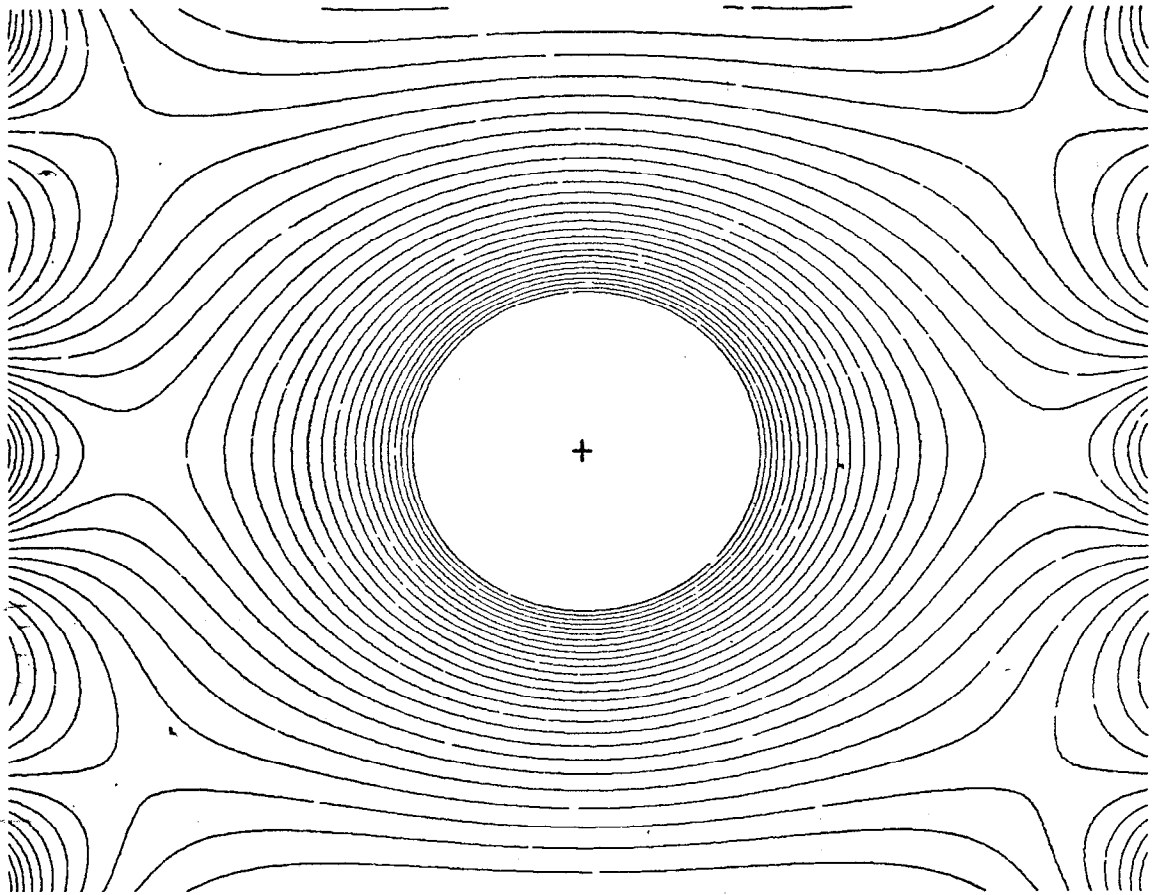
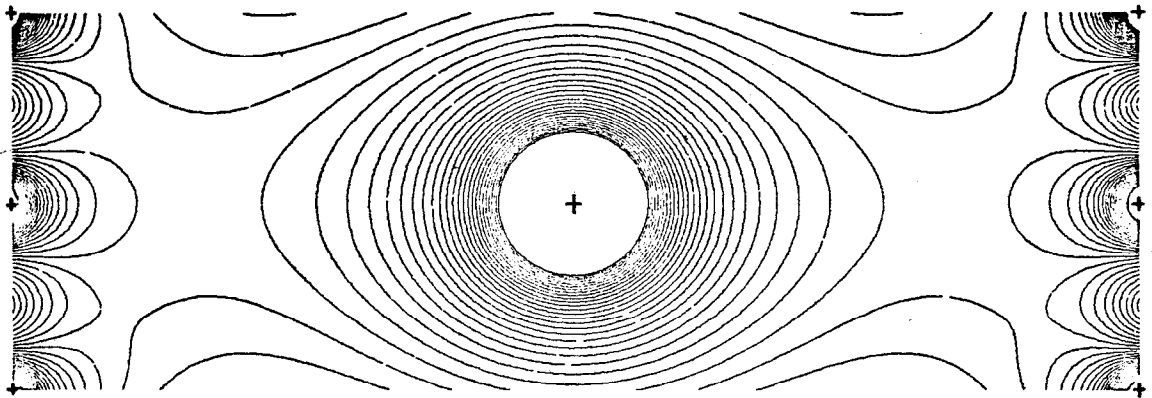


Fig. 3



(a)



(b)

8-78

341887

Fig. 4

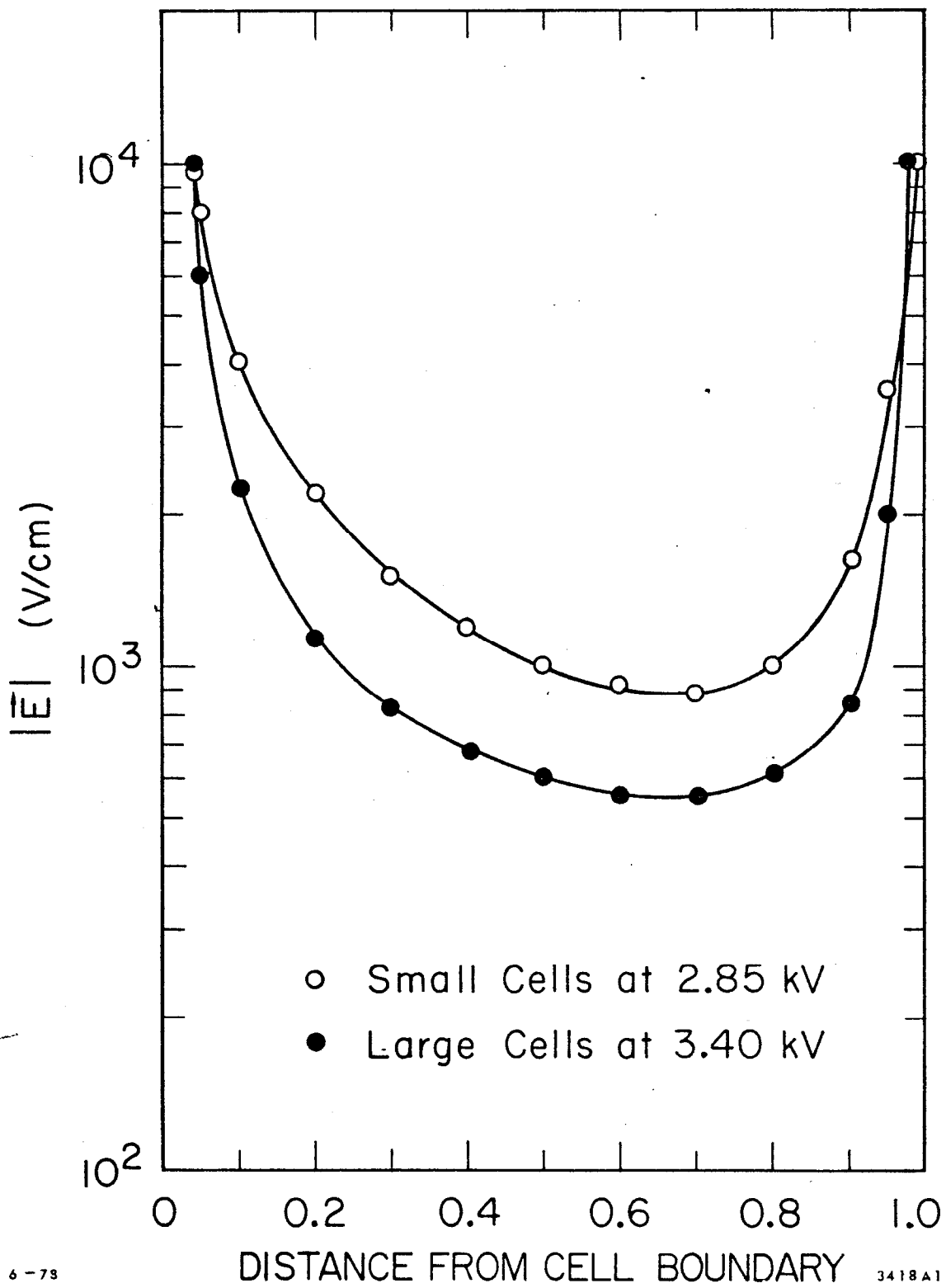
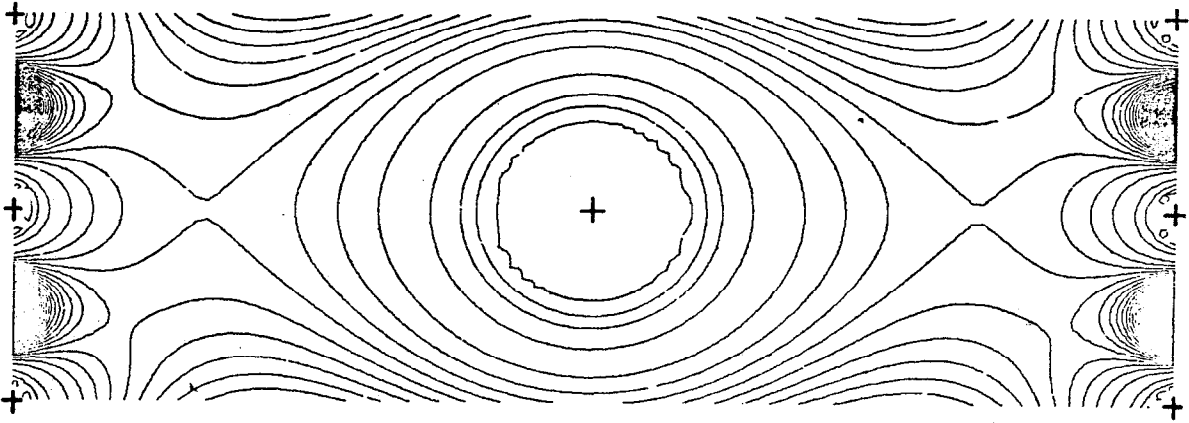
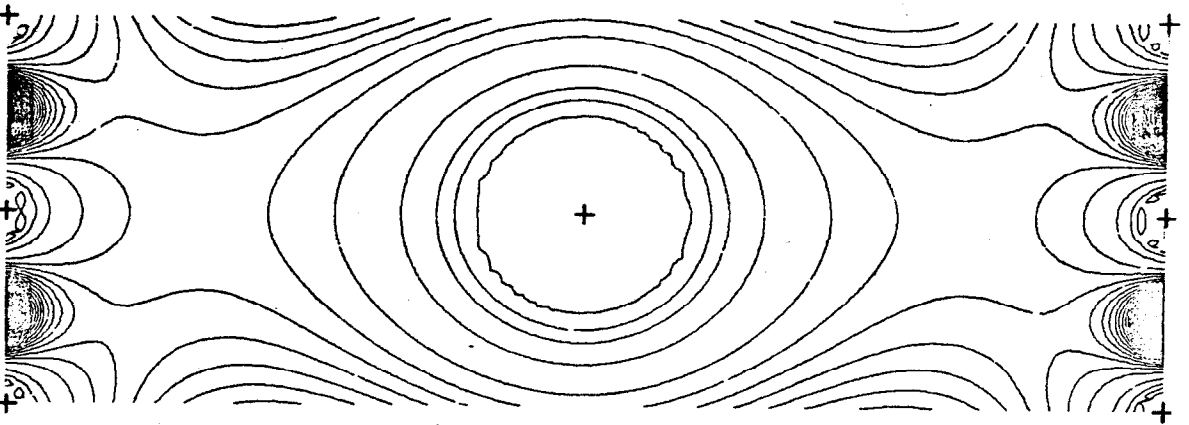


Fig. 5



(a)

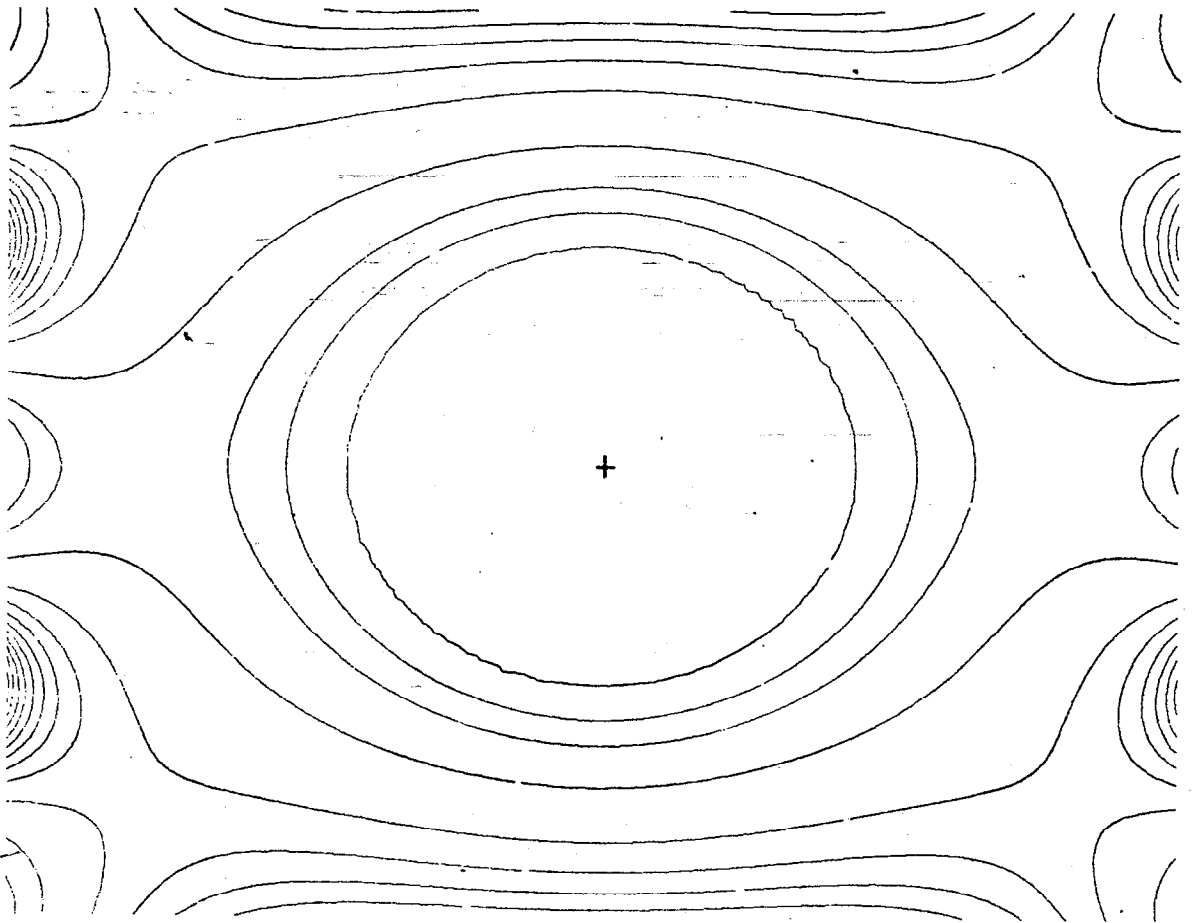


(b)

8-78

3418A5

Fig. 6



6-78

3418A1G

Fig. 7

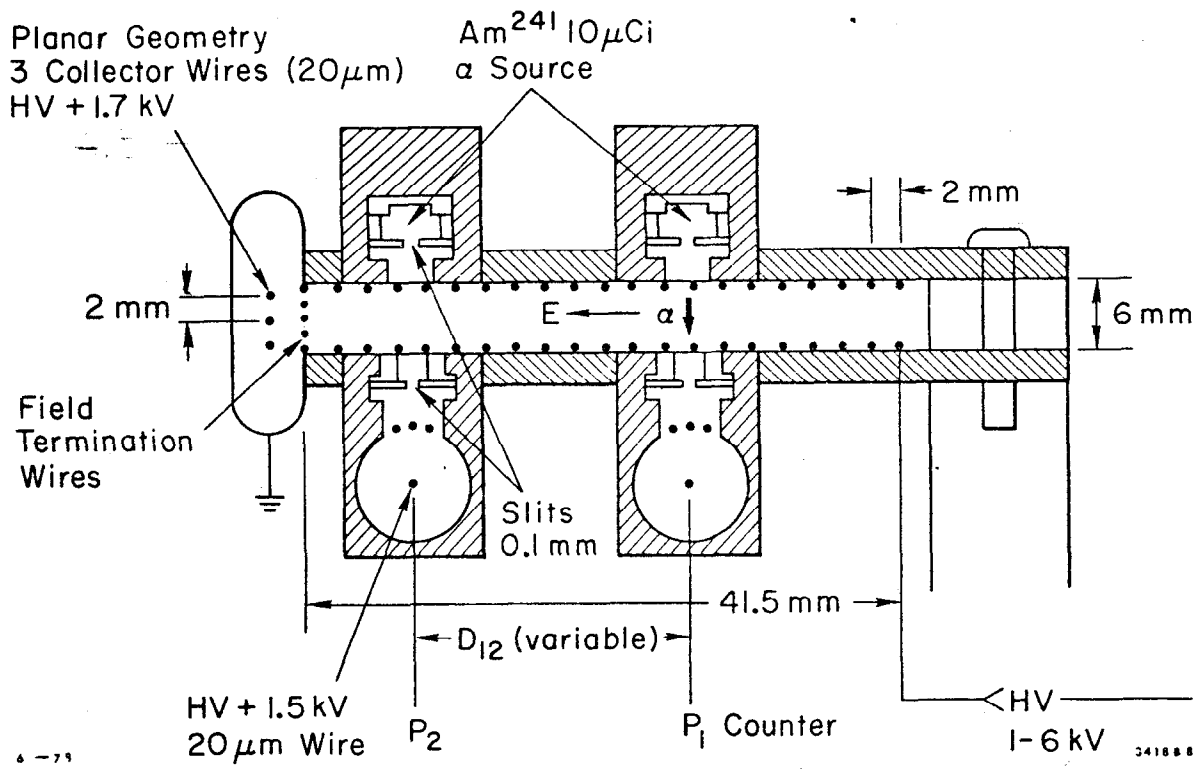


Fig. 8

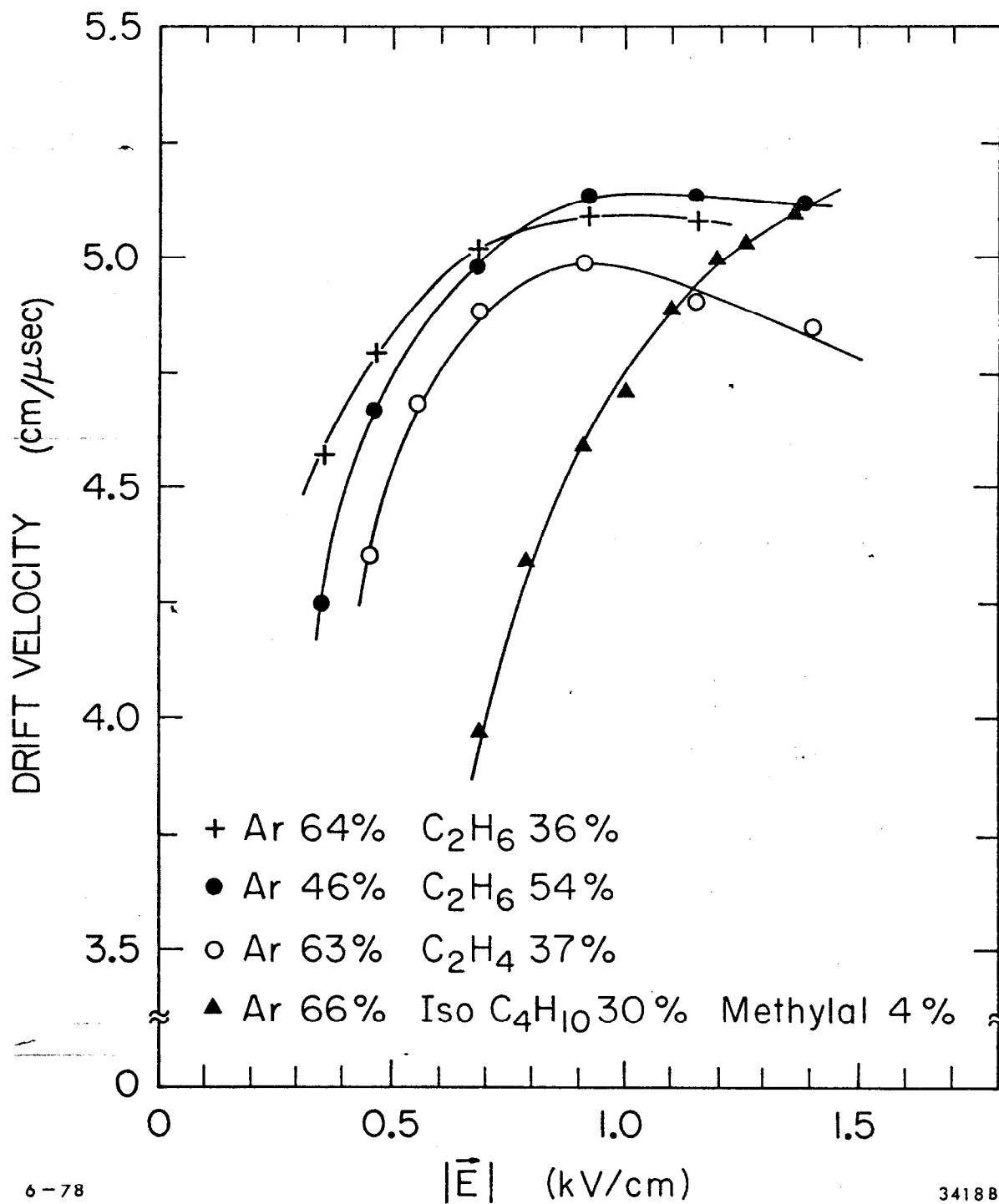


Fig. 9

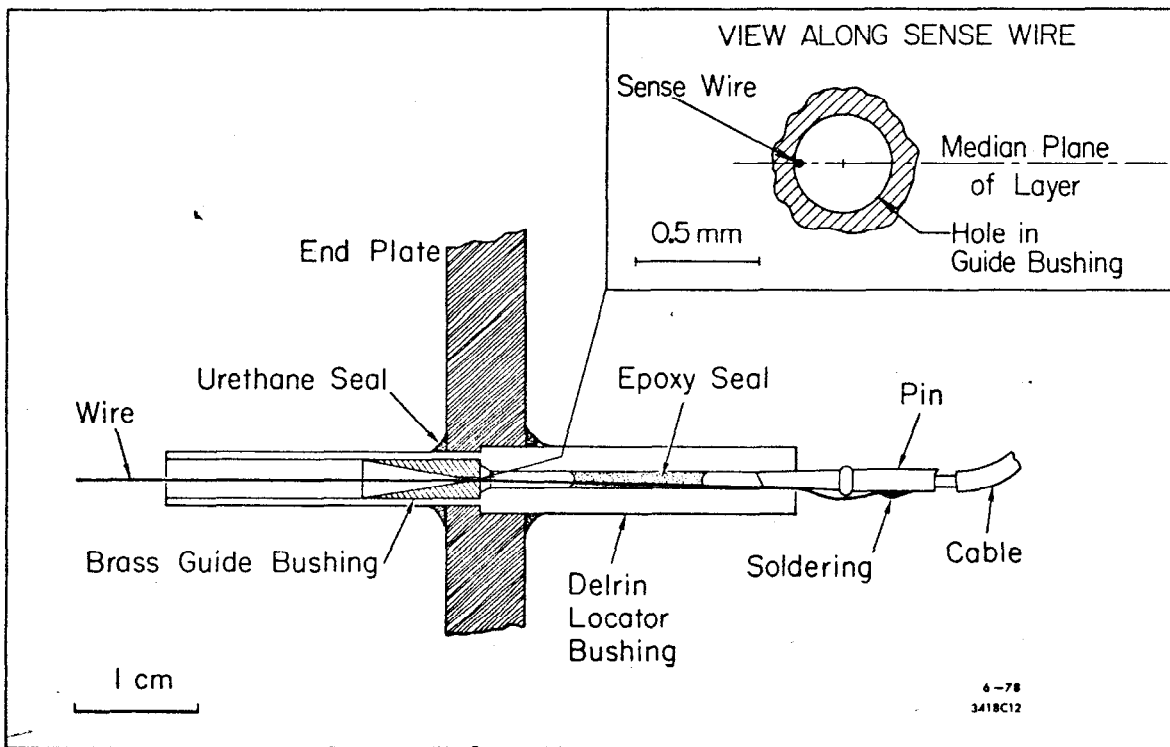


Fig. 10



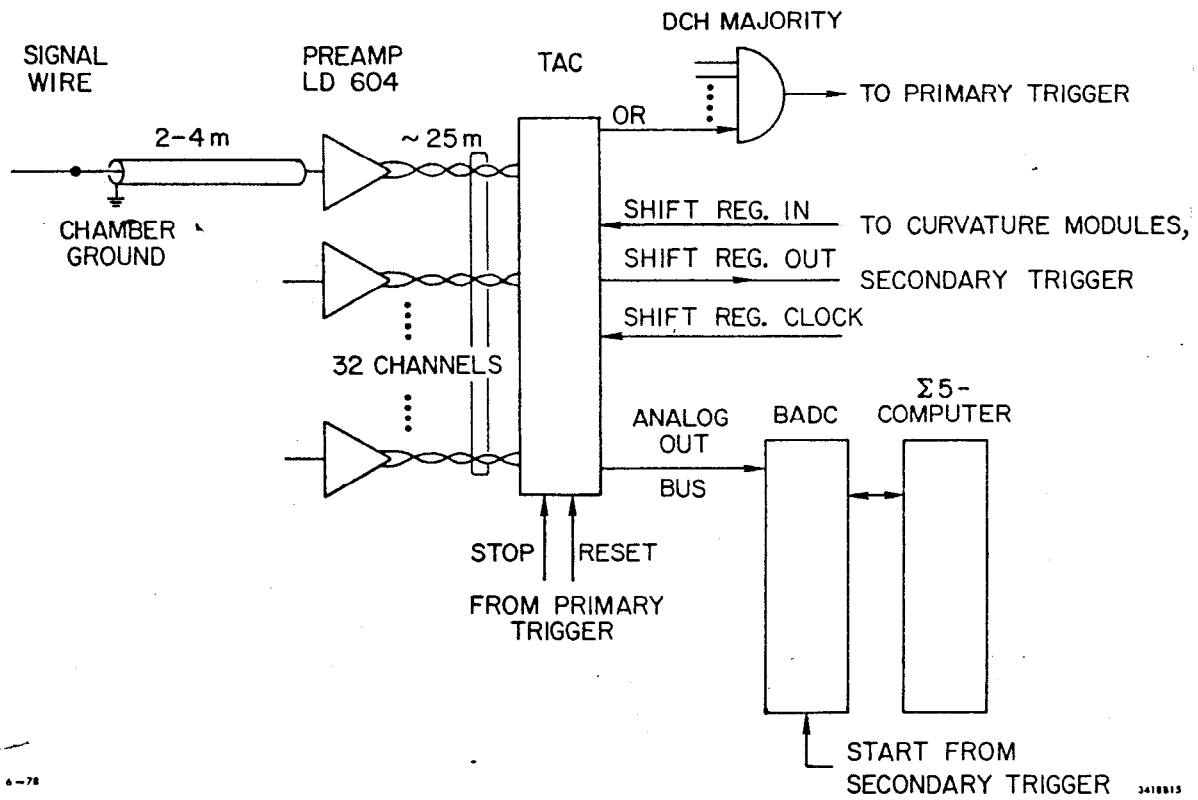


Fig. 11

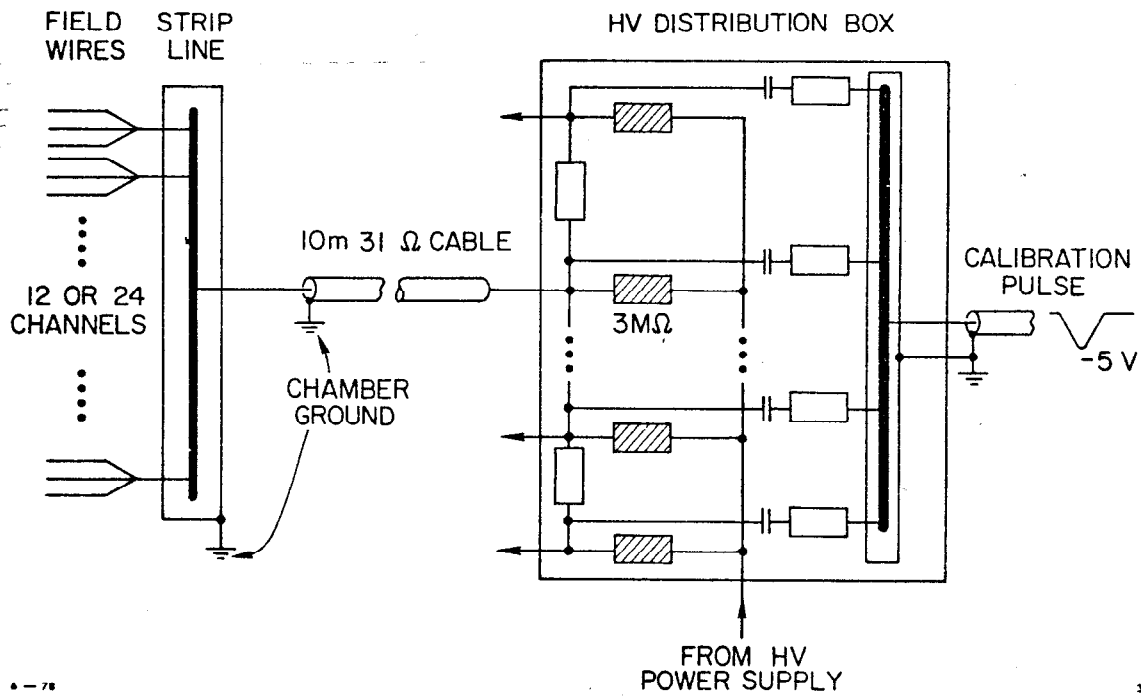


Fig. 12

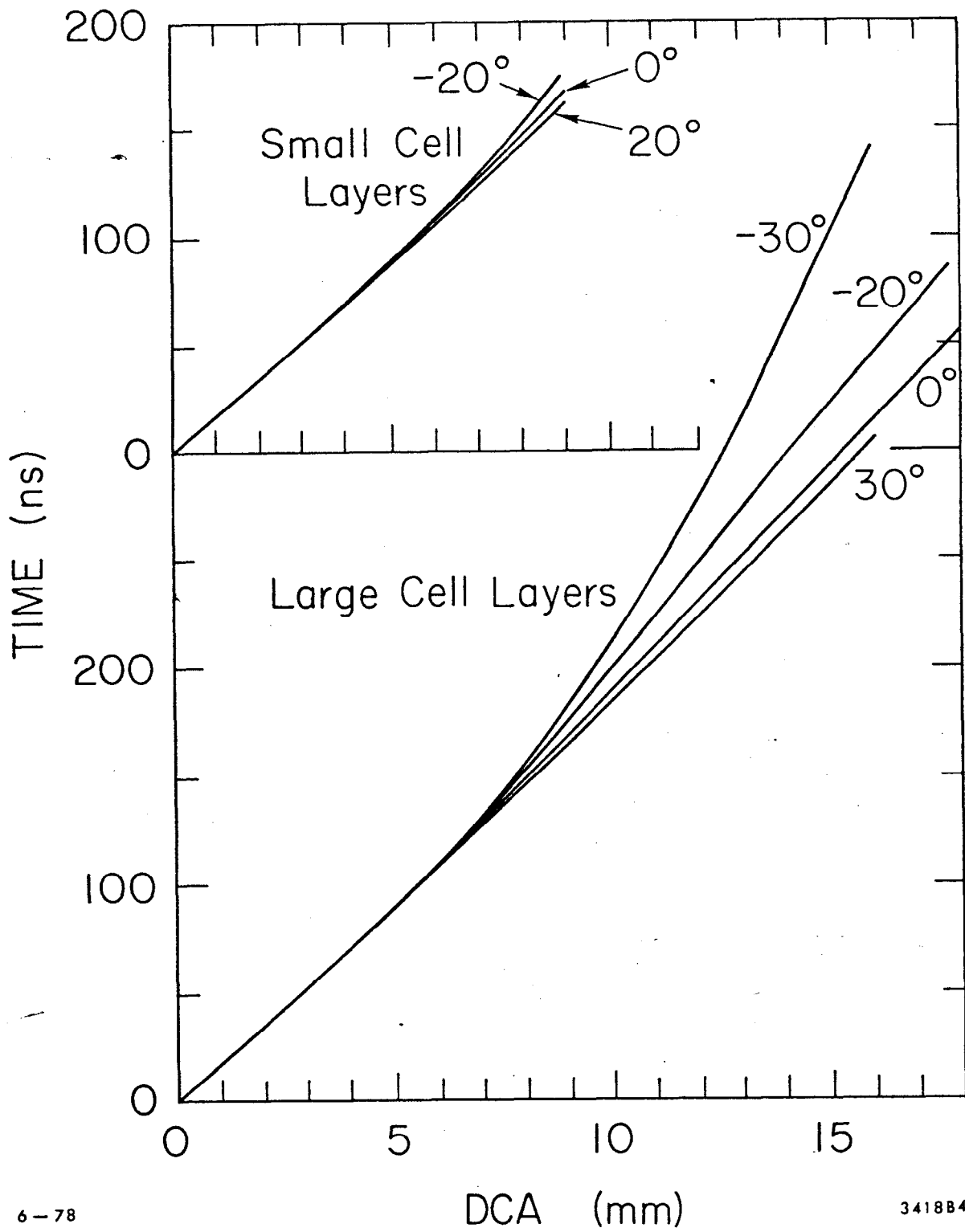
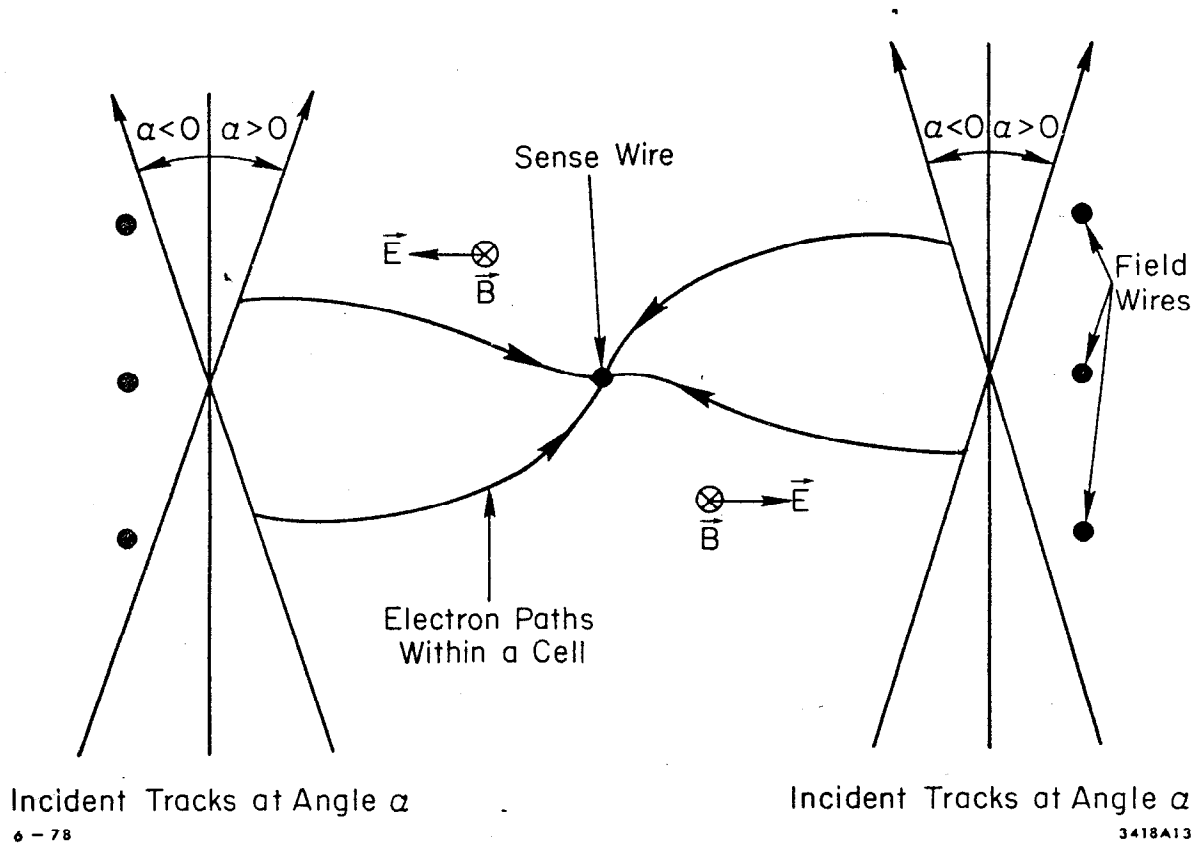


Fig. 13



Incident Tracks at Angle  $\alpha$   
6-78

Incident Tracks at Angle  $\alpha$   
3418A13

Fig. 14

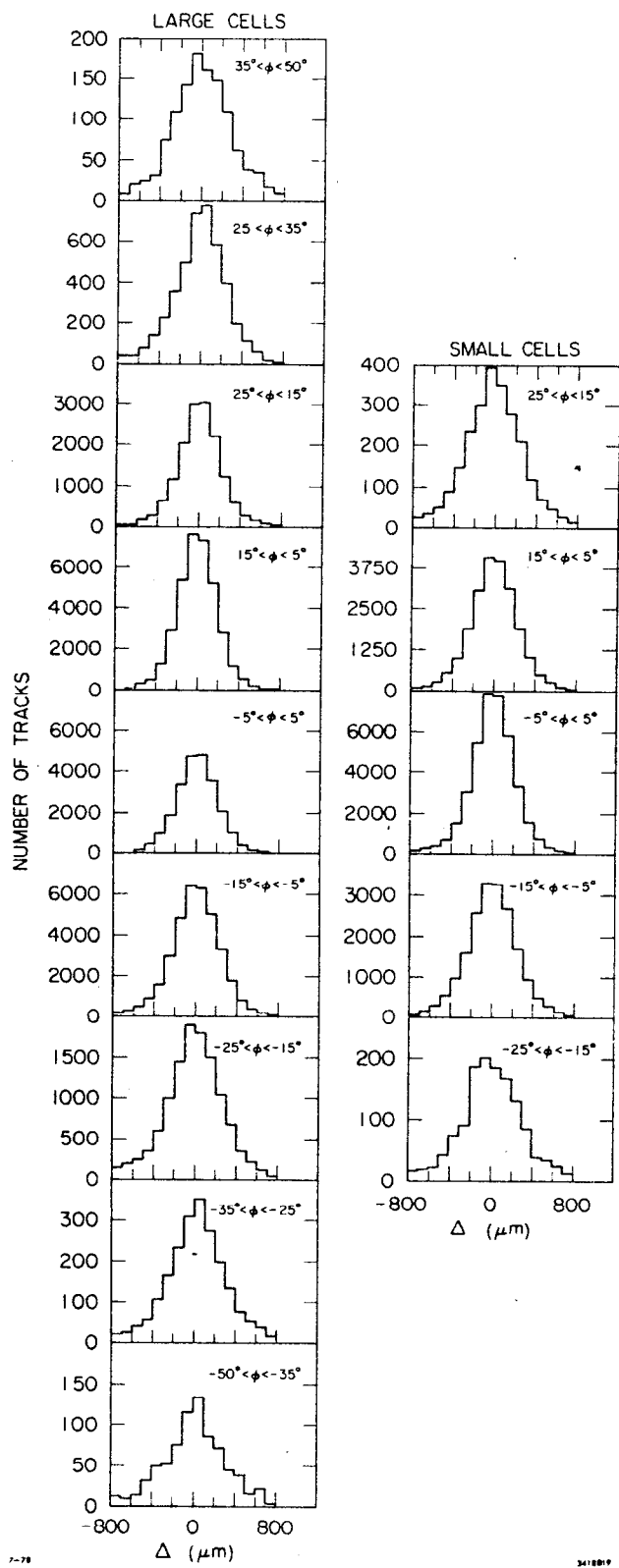
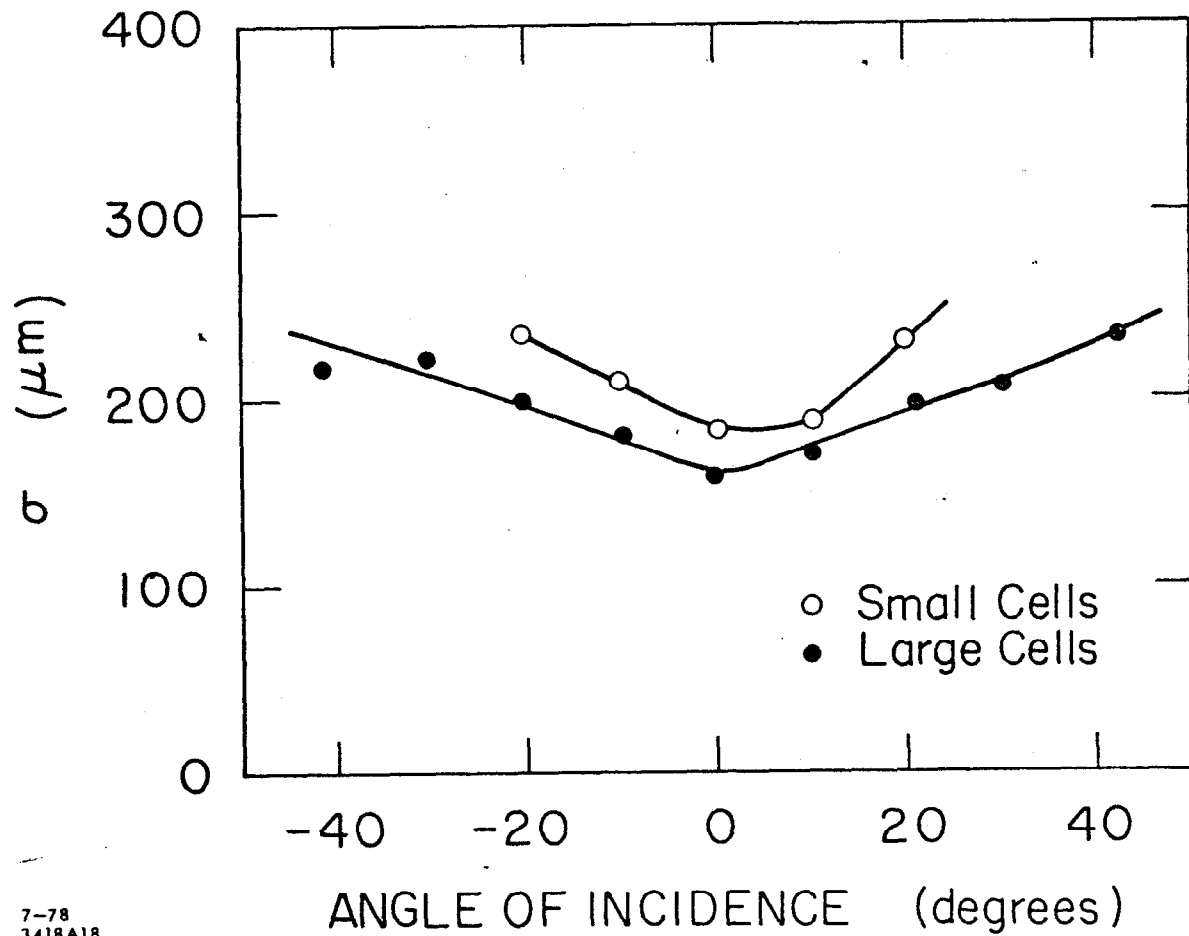
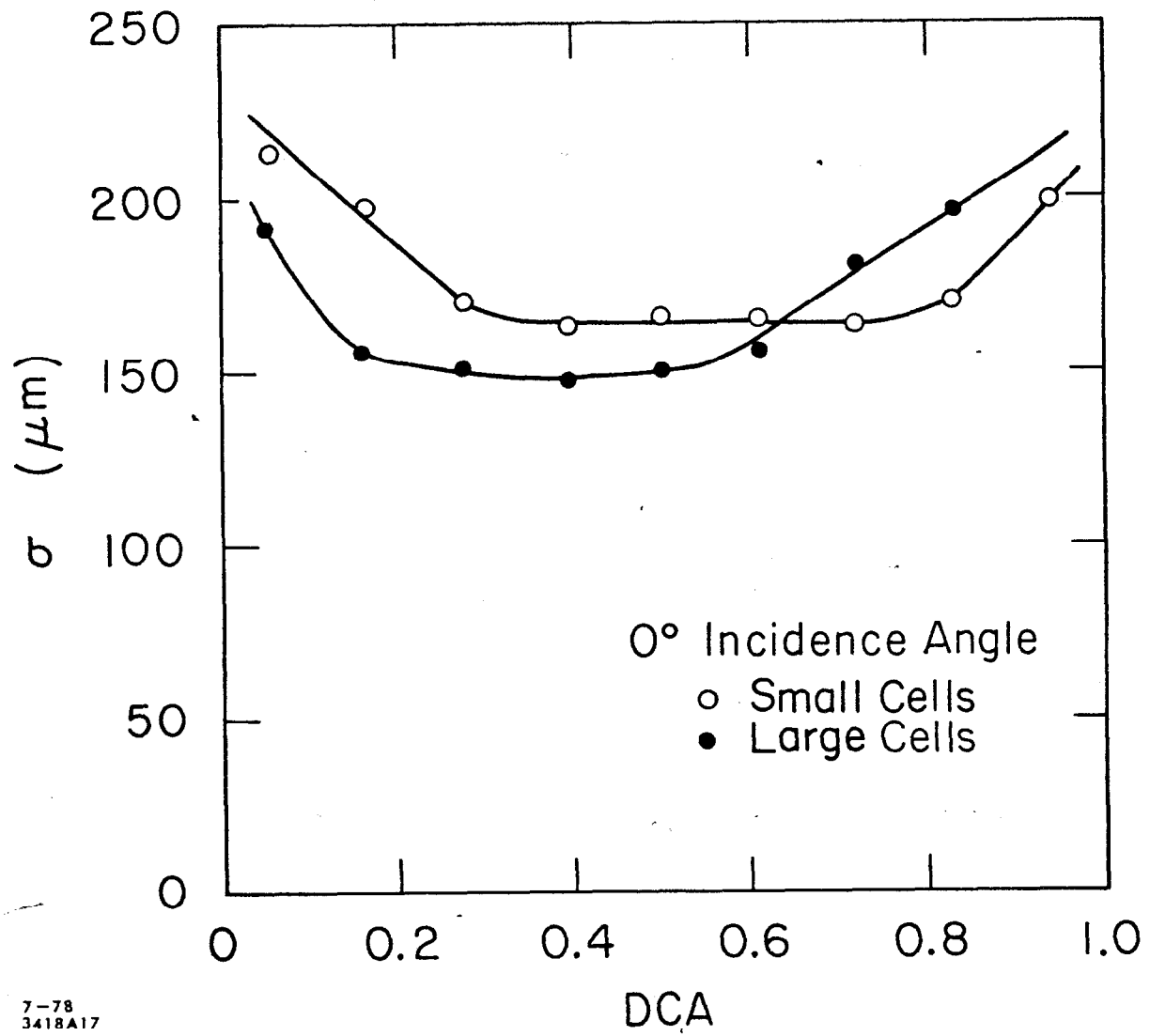


Fig. 15



7-78  
3418A18

Fig. 16



7-78  
3418A17

Fig. 17

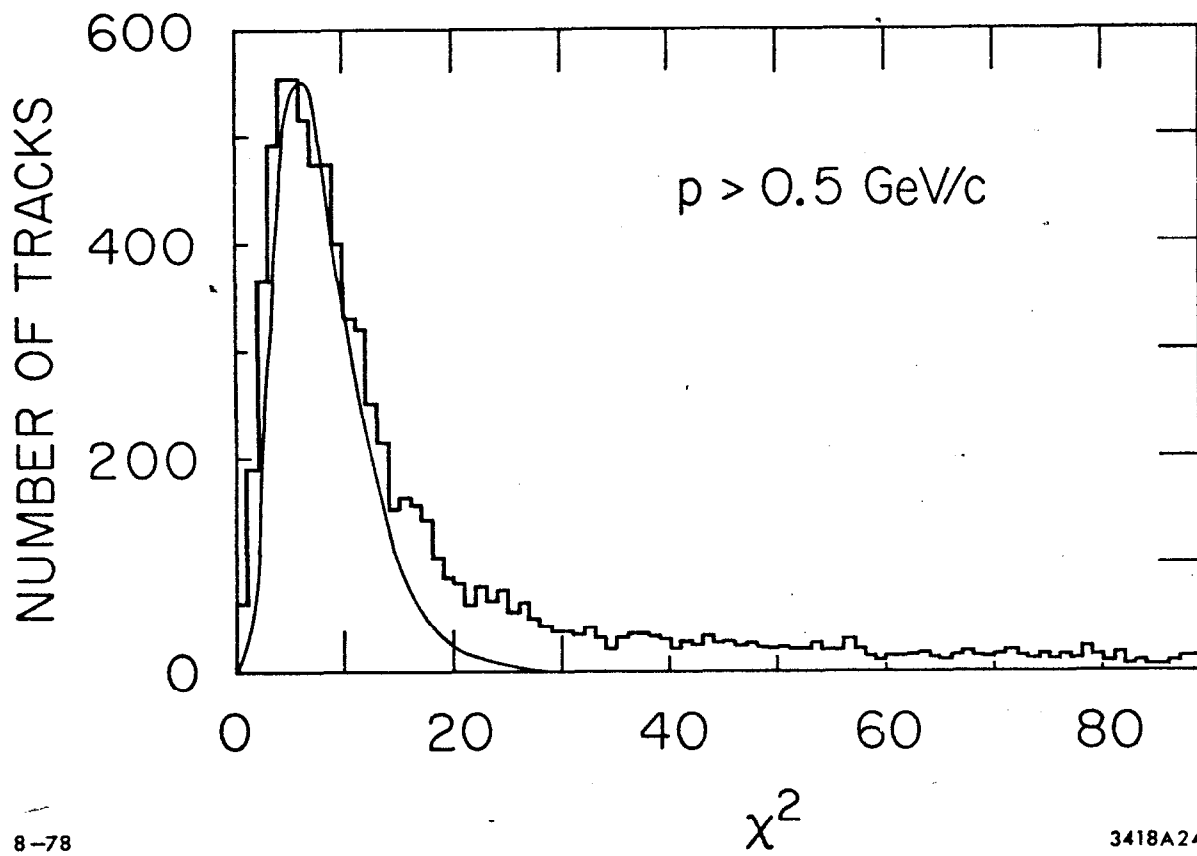


Fig. 18

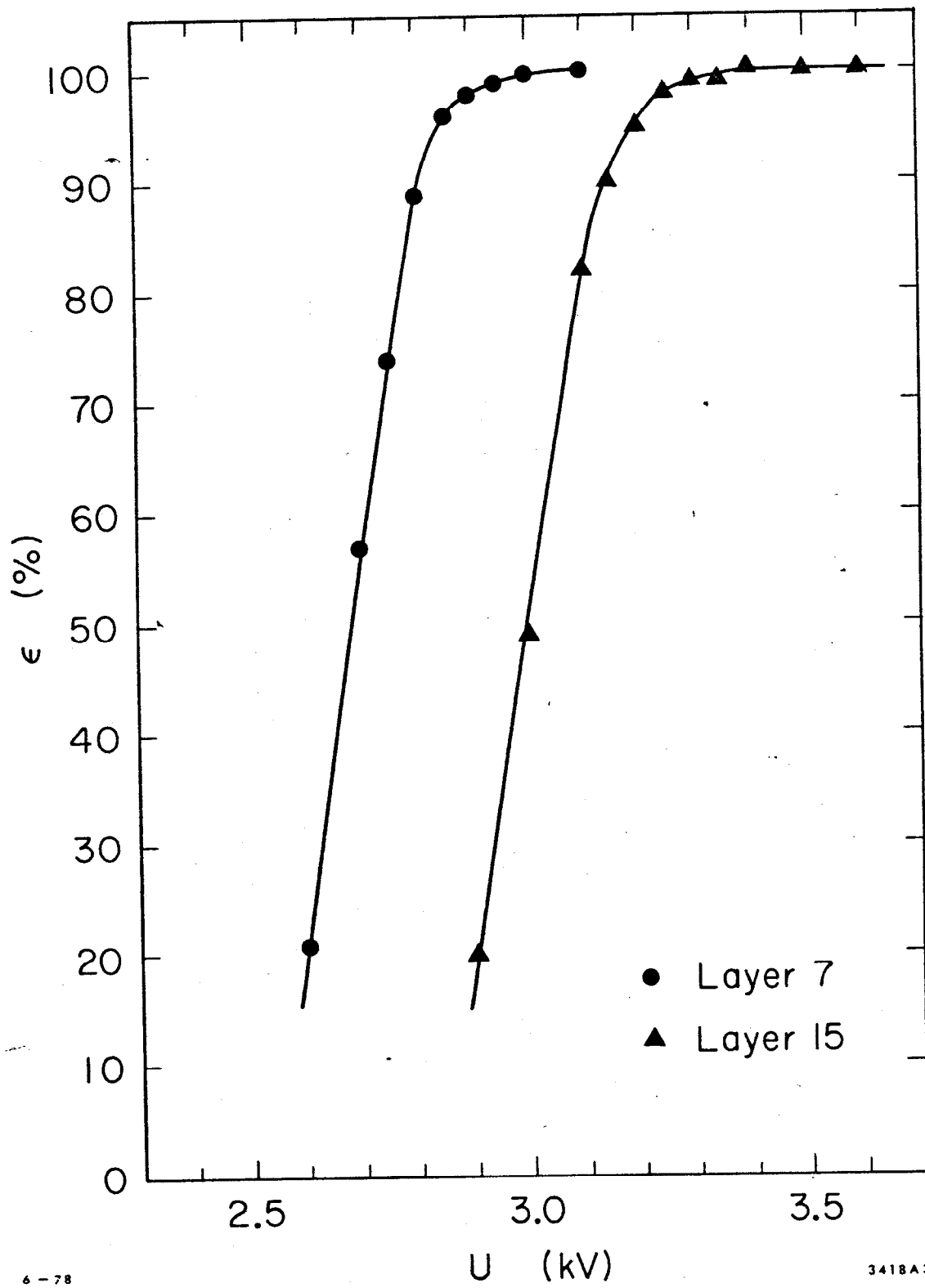


Fig. 19